

# Strong effects of time-dependent ionization in early SN 1987A<sup>\*</sup>

V. P. Utrobin<sup>1,2</sup> and N. N. Chugai<sup>3</sup>

<sup>1</sup> Max-Planck-Institut für Astrophysik, Karl-Schwarzschild-Str. 1, 85741 Garching, Germany

<sup>2</sup> Institute of Theoretical and Experimental Physics, B. Chermushkinskaya St. 25, 117259 Moscow, Russia  
e-mail: utrobin@itep.ru

<sup>3</sup> Institute of Astronomy of Russian Academy of Sciences, Pyatnitskaya St. 48, 109017 Moscow, Russia

Received 22 December 2004 / accepted 6 June 2005

**Abstract.** We study time-dependent hydrogen ionization in the atmosphere of SN 1987A during the first month after the supernova explosion. The model includes kinetics of hydrogen ionization and excitation, molecular hydrogen kinetics, and a time-dependent energy balance. The primary strong effect of the time-dependent ionization is the enhanced hydrogen ionization compared to the steady-state model. The time-dependent ionization provides a sufficient population of excited hydrogen levels to account for the observed H $\alpha$  without invoking the external <sup>56</sup>Ni. We find that the Ba II 6142 Å line in SN 1987A can be reproduced for the LMC barium abundance. This resolves the long-standing problem of the unacceptably high barium overabundance in SN 1987A. The key missing factor responsible for the “barium problem” is the time-dependent ionization. The modelling of the H $\alpha$  profile on day 4.64 indicates the ratio of the kinetic energy to the ejected mass  $\approx 0.83 \times 10^{50} \text{ erg } M_{\odot}^{-1}$ .

**Key words.** stars: supernovae: individual: SN 1987A – stars: supernovae: general

## 1. Introduction

Spectra of type IIP supernovae (SN) combined with photometric data are the primary source of our knowledge about the mass, energy, chemical composition, mixing and asymmetry of ejecta that are important for our understanding of the explosion mechanism. Generally, to recover the information from the spectra one needs to use complex models. Unfortunately, the ultimate model with all the physics included is beyond reach, so some simplifications are unavoidable. One of the assumptions accepted in the atmosphere models is the steady-state approximation for the ionization kinetics.

That the time-dependent effect of the hydrogen ionization may play a role in the SN envelope has been recognized by Kirshner & Kwan (1975); they applied this effect to account for the high H $\alpha$  luminosity of the type II SN 1970G. Time-dependent ionization has been invoked in SN 1987A to account for the high excitation of hydrogen in the outer atmosphere ( $v > 7000 \text{ km s}^{-1}$ ) during the first 40 days (Chugai 1991a). The crucial role of the time-dependent ionization at the late nebular epoch of SN 1987A has been emphasized by Clayton et al. (1992) and Fransson & Kozma (1993).

Recently, using a time-dependent model of the hydrogen ionization with the kinetics of atomic and molecular hydrogen we have found that time-dependent effects in SN 1987A were strong during the first month and that they could provide the hydrogen excitation required to account for the H $\alpha$  line strength

(Utrobin & Chugai 2002) which was underproduced in steady-state models of the SN 1987A atmosphere. However, our previous model has ignored the time-dependent energy balance; instead simple laws have been used to mimic the evolution of the electron temperature in the atmosphere.

Keeping in mind the importance of the non-steady state ionization effects for the understanding of the phenomena seen in early SN 1987A, we revisit this issue. To this end we upgrade the atmosphere model that in addition to the time-dependent kinetics also includes the time-dependent energy balance. Our main goal is to compute the ionization and excitation of hydrogen in the atmosphere of SN 1987A for different epochs, and to compare the calculated H $\alpha$  line with the observations. We also address the intriguing problem of high Ba overabundances that have been recovered by several studies (Mazzali et al. 1992, and references there). Our preliminary guess was that the Ba overabundance was caused by the strong underestimation of the Ba II ionization fraction.

We begin with a question: why time-dependent effects are important (Sect. 2) and then describe in detail the proposed model (Sect. 3). The H $\alpha$  strength on day 4.64 is used to constrain the kinetic energy of the hydrodynamic model Sect. 4.1, the computations of the ionization and temperature structure of the atmosphere along with the H $\alpha$  profiles for selected phases are presented in Sect. 4.2, while in Sect. 4.3 we address the problem of high Ba overabundance.

We adopt here the radial velocity of SN 1987A of  $286.5 \text{ km s}^{-1}$  (Meaburn et al. 1995) and the distance of 50 kpc.

<sup>\*</sup> Appendices A, B and C are only available in electronic form at <http://www.edpsciences.org>

## 2. Why time-dependent?

A widely shared view that the steady-state statistical equilibrium is a reasonable approximation for SN IIP atmospheres relies on the claim that the recombination time is much smaller than the SN age

$$(\alpha N_e)^{-1} \ll t, \quad (1)$$

where  $\alpha$  is the coefficient of recombination to the excited states,  $N_e$  is the electron number density. Adopting  $\alpha \sim 3 \times 10^{-13} \text{ cm}^3 \text{ s}^{-1}$  and a typical SN age at the photospheric epoch  $t \sim 10^6\text{--}10^7 \text{ s}$  one finds that the requirement (1) is satisfied for  $N_e \gg 10^7 \text{ cm}^{-3}$ . This condition is met near the photosphere thus supporting, at first glance, the steady-state approximation. Meanwhile, it is violated in the outer, high velocity layers, where  $N_e$  may drop as low as  $10^7 \text{ cm}^{-3}$ . Therefore, generally, the time-dependent approach is needed, at least if one addresses the situation in the outer layers.

Moreover, it turns out that the steady-state approximation is violated also in the inner atmosphere, where the condition (1) holds. This inequality has little in common with the condition of the steady state for a multilevel atom irradiated by the optical continuum, because of the efficient reionization of the recombined atom. The importance of this phenomenon has been recognized for the problem of hydrogen recombination in the early universe, where  $L\alpha$  trapping along with the reionization from the second level results in a significant increase of the recombination time  $t_{\text{rec}} = -N_e/(dN_e/dt)$  (Zeldovich et al. 1968).

The net recombination rate  $dN_e/dt$  refers to transitions to the ground state that either do not emit  $L\alpha$  or are followed by the escape of the emitted  $L\alpha$  quantum without resonance scattering. Let the probability of such a transition be  $w_{21}$ . Then in the ‘‘two level plus continuum’’ approximation the net recombination rate (neglecting the expansion effect) is

$$\frac{dN_e}{dt} = -\alpha N_e^2 w_{21}. \quad (2)$$

With all the major processes from the second level taken into account the probability  $w_{21}$  is

$$w_{21} = \frac{A_{2q} + N_e q_{21} + A_{21} \beta_{21}}{P_2 + A_{2q} + N_e q_{21} + A_{21} \beta_{21}}, \quad (3)$$

where  $P_2$  is the photoionization rate from the second level;  $A_{2q}$  is the probability of the two-photon decay evaluated for the equipartition of 2s and 2p levels;  $q_{21}$  is the collisional de-excitation coefficient;  $A_{21} \beta_{21}$  is the  $L\alpha$  escape probability.

Let us estimate  $w_{21}$  for the neutral hydrogen number density  $N_1 > 10^9 \text{ cm}^{-3}$  and the electron number density  $N_e < 10^8 \text{ cm}^{-3}$ , when the two-photon transition dominates over collisional transition and  $L\alpha$  escape, i.e.,  $w_{21} \approx A_{2q}/P_2$ . This situation is typical for the inner atmosphere of SN IIP. With the photospheric temperature of  $T \approx 5000 \text{ K}$  one gets  $P_2 \approx 10^4 \text{ W s}^{-1}$ , where  $W$  is the dilution factor. Close to the photosphere (for  $W > 0.1$ ) one finds  $w_{21} < 2 \times 10^{-3}$ . The effective recombination time is then

$$t_{\text{rec}} = -N_e/(dN_e/dt) = 1/(\alpha N_e w_{21}) \sim 500/(\alpha N_e). \quad (4)$$

This shows that the effective recombination time is by a factor of  $1/w_{21} \sim 500$  greater than the recombination time to excited

states  $1/(\alpha N_e)$ . For  $N_e \sim 10^8 \text{ cm}^{-3}$  one obtains  $t_{\text{rec}} > 10^7 \text{ s} > t$ . We thus conclude that the steady-state approximation may break down in the dense inner atmosphere as well.

These qualitative considerations demonstrate that the hydrogen recombination in the atmosphere of SN IIP at the photospheric epoch is essentially a time-dependent phenomenon.

## 3. The model and input physics

A self-consistent treatment of the SN atmosphere requires hydrodynamic modelling with time-dependent radiation transport, energy balance and ionization kinetics. At present such a general approach is beyond reach of computational possibilities. To study time-dependent effects in the atmosphere of SN 1987A and yet to make the problem solvable, we do not consider the radiation transfer in the atmosphere, using, instead, a simple description of the continuum radiation field.

### 3.1. Continuum radiation

The SN atmosphere is very opaque in the Lyman continuum ( $\nu \geq \nu_1$ ), so the contribution of the photospheric Lyman continuum can be neglected and the radiation field in this frequency band is fully determined by the diffusive continuum produced by hydrogen recombinations and free-free emission. Therefore, in the optically thick medium the average intensity of the Lyman continuum is

$$J_\nu = \frac{\eta_1^{\text{bf}}(\nu) + \eta^{\text{ff}}(\nu)}{\kappa_1^{\text{bf}}(\nu) + \kappa^{\text{ff}}(\nu)} \quad \text{for } \nu \geq \nu_1. \quad (5)$$

Here  $\eta_1^{\text{bf}}(\nu)$  and  $\kappa_1^{\text{bf}}(\nu)$  are the monochromatic thermal emissivity due to hydrogen recombination to the ground level and the monochromatic true absorption coefficient of the hydrogen ground level corrected for stimulated emission;  $\eta^{\text{ff}}(\nu)$  and  $\kappa^{\text{ff}}(\nu)$  are the monochromatic thermal emissivity including free-free processes for all atoms and ions and the monochromatic true free-free absorption coefficient corrected for stimulated emission, respectively (Mihalas 1978). As we will see below (Sect. 4.2) the time-dependent ionization degree in the atmosphere exceeds the equilibrium value predicted by the Saha equation for the local electron temperature. Therefore the average intensity of the Lyman continuum in the atmosphere is greater than the equilibrium value given by the Planck function,  $B_\nu(T_e)$ , and the radiation field in continuum at these frequencies is not in thermal equilibrium with matter.

At the lower frequencies between the Balmer and Lyman edges ( $\nu_2 \leq \nu < \nu_1$ ) the ultraviolet (UV) radiation interacts with numerous metal lines and, as a result, there is the large optical depth due to the corresponding line opacity. Note that the scattering of UV metal lines is liable to photon splitting and this interaction will be close to the absorption rather than scattering. In the case of the purely absorbing extended atmosphere with the constant absorption coefficient independent of wavelength the radiation field is described by the solution of Chandrasekhar (1934). We use this approximation for the UV band with the effective optical depth of unity.

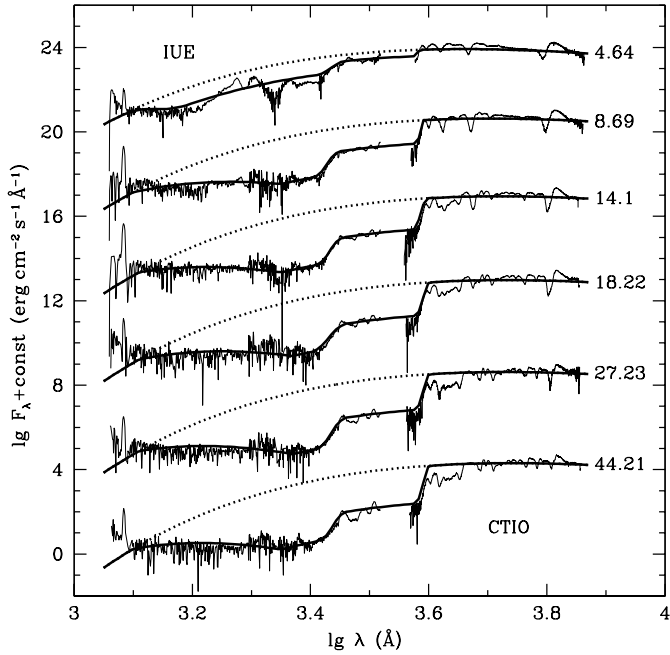


**Fig. 1.** The combined UV (IUE) (Pun et al. 1995) and optical (CTIO) (Phillips et al. 1988) spectra of SN 1987A (*thin solid line*), the black-body continuum at the calculated effective temperature of the high-energy model (*dotted line*), and the observed continuum (*thick solid line*) between days 4.64 and 44.21.

In the visual band ( $\nu < \nu_2$ ), where the optical depth of the atmosphere is quite low, we adopt the free-streaming approximation – the important simplification in evaluating the continuum radiation field. This approximation gives the average intensity of the continuum in the atmosphere as a simple relation  $J_\nu = WI_\nu$ , where  $I_\nu$  is the specific intensity of the photospheric radiation. The photospheric radius  $R_{\text{ph}}$  and effective temperature  $T_{\text{eff}}$  are provided by the hydrodynamic model.

To further allow for the uncertainty of our approximation we consider two extreme cases: (i) the photospheric brightness is black-body with the effective temperature (model A); (ii) the photospheric brightness corresponds to the observed spectrum (model B) (Fig. 1). The real situation is somewhere between these two cases.

### 3.2. Hydrodynamic model

The density distribution, chemical composition, radius of the photosphere and effective temperature are provided by the hydrodynamic model of SN 1987A (see for details Utrobin 2004). We consider the non-evolutionary model N of Utrobin (2004) with  $18 M_\odot$  ejecta, kinetic energy of  $10^{51}$  erg, and  $^{56}\text{Ni}$  mass of  $0.073 M_\odot$ . For the distance modulus to the LMC of  $m - M = 18.5$  mag, color excess of  $E(B - V) = 0.15$  mag, and an interstellar extinction of  $A_V = 3.1E(B - V)$  mag the progenitor of SN 1987A, Sanduleak  $-69^\circ 202$ , had a radius of  $46.8 R_\odot$ . To produce the presupernova density distribution, the evolutionary model l20n2ae of Woosley et al. (1997) was rescaled to the adopted radius and ejecta mass. We assumed for the outer layers the circumstellar helium abundance  $Y = 0.441$

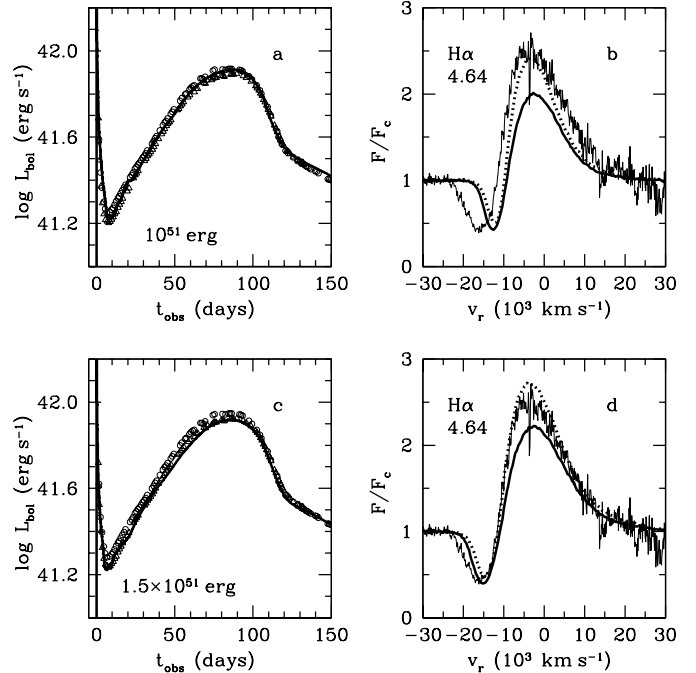


**Fig. 2.** Comparison of the low and high-energy models of SN 1987A. *Top: a)* bolometric light curve of the low-energy model (*thick solid line*) compared with the observations of SN 1987A obtained by Catchpole et al. (1987, 1988) (*open circles*) and Hamuy et al. (1988) (*open triangles*), and *b)* the  $\text{H}\alpha$  line profile on day 4.64 computed on the basis of this hydrodynamic model for the black-body continuum (model A) (*dotted line*) and the observed continuum (model B) (*thick solid line*). The calculated spectra are overplotted on the observed spectrum (Phillips et al. 1988) (*thin solid line*). *Bottom: c)* bolometric light curve of the high-energy model and *d)* the corresponding  $\text{H}\alpha$  profile on day 4.64.

(Wang 1991; Lundqvist & Fransson 1996) and the LMC metallicity  $Z = 0.004$  (Dufour 1984). The structure of the presupernova outer layers was modified to increase the density compared with the evolutionary model of a non-rotating single star. This correction was needed to fit the observed bolometric light curve of SN 1987A (Fig. 2a) with a moderate mixing of radioactive  $^{56}\text{Ni}$  in the velocity range  $\leq 2500 \text{ km s}^{-1}$  (Utrobin 2004). The final model is called the low-energy model.

We consider also the high-energy version of the above model. This model with the kinetic energy  $1.5 \times 10^{51}$  erg differs from the low-energy model by the presupernova radius of  $35.0 R_\odot$ ,  $^{56}\text{Ni}$  mass of  $0.0765 M_\odot$ , and the adopted color excess of  $E(B - V) = 0.17$  mag (Michael et al. 2003). The chemical composition of the outer layers is typical of the LMC chemical composition,  $X = 0.743$ ,  $Y = 0.251$  and  $Z = 0.006$  (Dufour 1984). This model agrees with the observed bolometric light curve of SN 1987A for  $^{56}\text{Ni}$  mixed in the velocity range  $\leq 3000 \text{ km s}^{-1}$  (Fig. 2c).

### 3.3. Line transfer

Starting the first day the envelope of SN 1987A expands homogeneously (Utrobin 2004), so the Sobolev approximation is

applicable. In this approximation the line transfer is described by the escape probability (Sobolev 1960; Castor 1970)

$$\beta_{ul} = \frac{1 - \exp(-\tau_{lu})}{\tau_{lu}}, \quad (6)$$

where

$$\tau_{lu} = \frac{\pi e^2}{m_e c} f_{lu} \lambda_{lu} \left( N_l - \frac{g_l}{g_u} N_u \right) \quad (7)$$

is the Sobolev optical depth in a transition from level  $l$  to level  $u$ . Here  $N_l$ ,  $g_l$ ,  $N_u$ ,  $g_u$  are number densities and statistical weights of atoms in the lower and upper levels, respectively,  $f_{lu}$  is the oscillator strength, and  $\lambda_{lu}$  is the line wavelength. In the Sobolev approximation the frequency-averaged mean intensity of the line is

$$J_{lu} = (1 - \beta_{ul}) S_{lu} + \beta_{ul} J(\nu_{lu}), \quad (8)$$

where

$$S_{lu} = \frac{2h\nu_{lu}^3}{c^2} \left( \frac{g_u N_l}{g_l N_u} - 1 \right)^{-1} \quad (9)$$

is the line source function and  $\nu_{ul}$  is the line frequency. The net frequency-integrated line emissivity is

$$\eta_{ul} = \frac{1}{4\pi} h\nu_{lu} N_u A_{ul} \beta_{ul} \left( 1 - \frac{J(\nu_{lu})}{S_{lu}} \right), \quad (10)$$

where  $A_{ul}$  is the Einstein spontaneous emission probability for the transition from level  $u$  to level  $l$ .

For the very opaque  $L\alpha$  line the Sobolev approximation is violated if one considers the  $L\alpha$  radiation transfer, but remains valid if one is interested in the computations of the escape rate (Chugai 1980). The  $L\alpha$  quanta may be lost between scatterings also owing to the selective absorption in Fe II lines. This process has been invoked for pumping to Fe II levels in cool giant atmospheres (Johansson & Jordan 1984). The Fe II transitions responsible for the absorption of  $L\alpha$  quanta have the lower term  $a^4D$  with the excitation potential of  $\sim 1$  eV, that may be excited in dense warm layers of the SN 1987A atmosphere. To estimate the role of this process we rely on the probability of the  $L\alpha$  loss due to escape and selective absorption with the partial frequency redistribution taken into account (Chugai 1998). Although the latter probability has been obtained for a single line, the effect of numerous lines can be also easily estimated since the contribution of lines in the relevant frequency range is additive. The list of Fe II lines responsible for the selective absorption of  $L\alpha$  is taken from Johansson & Jordan (1984).

### 3.4. Gamma-rays and positrons deposition

The gamma rays with energy of about 1 MeV from the decay chain  $^{56}\text{Ni} \rightarrow ^{56}\text{Co} \rightarrow ^{56}\text{Fe}$  deposit their energy through Compton scattering by free and bound electrons. The Compton electrons lose their energy through the Coulomb heating of free electrons and the ionization and excitation of atoms and ions. The rates of the heating, non-thermal ionization and excitation for atoms and ions are taken according to Kozma & Fransson (1992). The gamma-ray transport is calculated in the approximation of the effective absorption opacity of  $0.06 Y_e \text{ cm}^2 \text{ g}^{-1}$ , where  $Y_e$  is the number of electrons per baryon. Positrons are assumed to deposit their energy locally.

### 3.5. Rate equations

The following elements and molecules are calculated in time-dependent non-LTE chemical kinetics: H, He, C, N, O, Ne, Na, Mg, Si, S, Ar, Ca, Fe, Ba,  $\text{H}^-$ ,  $\text{H}_2$ ,  $\text{H}_2^+$  and  $\text{H}_3^+$ . All elements but H are treated with the three ionization stages. Neutral hydrogen and ions Mg II, Fe II and Ba II are modelled with 15, 9, 30 and 17 levels, respectively, while other atoms and ions are assumed to consist of the ground state and continuum. The reaction network includes all bound-bound and bound-free, radiative and collisional processes for the atoms and ions with a detailed level structure (Appendices A.1–A.4), all bound-free, radiative and collisional processes for the two-state atoms and ions (Appendix A.5). We consider kinetics of hydrogen molecules that may affect the hydrogen ionization degree. Seven radiative and 37 collisional processes for the molecules are taken into account (Appendices B.1, B.2).

For one-dimensional, spherically symmetric flow the equation of continuity simplifies to

$$\frac{\partial \rho}{\partial t} = -\frac{\rho}{t_{\text{exp}}}, \quad \frac{1}{t_{\text{exp}}} = \left( 2 + \frac{\partial \ln v}{\partial \ln r} \right) \frac{v}{r}, \quad (11)$$

where  $\partial/\partial t$  is the Lagrangean time derivative;  $\rho$  is the density of the matter;  $r$  and  $v$  are radius and velocity, respectively. The net rate of transitions between level  $k$  and all other levels of neutral atom  $z$  by atomic processes is

$$\begin{aligned} \left[ \frac{\partial N_{z^0,k}}{\partial t} \right] &= \sum_{u>k} N_{z^0,u} A_{uk} \left( 1 - \frac{J_{lu}}{S_{ku}} \right) + N_{z^+} N_e \alpha_k \\ &\quad - N_{z^0,k} \sum_{l<k} A_{kl} \left( 1 - \frac{J_{lu}}{S_{lk}} \right) - N_{z^0,k} P_k \\ &\quad + N_e \sum_{u>k} (N_{z^0,u} q_{uk} - N_{z^0,k} q_{ku}) + N_{z^+} N_e^2 q_{c,k} \\ &\quad - N_e \sum_{l<k} (N_{z^0,k} q_{kl} - N_{z^0,l} q_{lk}) - N_e N_{z^0,k} q_{k,c} \\ &\quad + R_k^\gamma - R_{k,c}^\gamma, \end{aligned} \quad (12)$$

where  $N_{z^0,k}$  is the number density of neutral atom  $z$  at the level  $k$ ;  $N_{z^+}$  is the number density of singly ionized element  $z$ ;  $N_e$  is the number density of free electrons;  $J_{lu}$  is the frequency-averaged mean intensity of the line (8);  $S_{lu}$  is the line source function (9);  $\alpha_k$  and  $P_k$  are the total radiative recombination coefficient, including the spontaneous and induced processes, and the photoionization rate of the neutral atom  $z$  in level  $k$ , respectively (Mihalas 1978);  $q_{lu}$  is the electron collisional excitation rate from level  $l$  to level  $u$ ;  $q_{ul} = (N_{z^0,l}/N_{z^0,u})^* q_{lu}$  is the corresponding deexcitation rate and the ratio  $(N_{z^0,l}/N_{z^0,u})^*$  for the local thermodynamic equilibrium (LTE) is given by the Boltzmann formula;  $q_{k,c}$  is the electron collisional ionization rate from level  $k$ ;  $q_{c,k} = (N_{z^0,k}/N_{z^+} N_e)^* q_{k,c}$  is the corresponding recombination coefficient and the LTE ratio  $(N_{z^0,k}/N_{z^+} N_e)^*$  is given by the Saha equation;  $R_k^\gamma$  and  $R_{k,c}^\gamma$  are the non-thermal excitation and ionization rates of the neutral atom  $z$  in level  $k$ , respectively (Kozma & Fransson 1992).

The rate equation for the number density  $N_{\text{H}^0,2}$  of neutral hydrogen in level 2 is determined by the net rate of flow of particles into the unit volume with a characteristic time  $t_{\text{exp}}$  (11),

the net rate (12), hydrogen two-photon decays and other depopulation processes:

$$\begin{aligned} \frac{\partial N_{\text{H}^0,2}}{\partial t} = & -\frac{N_{\text{H}^0,2}}{t_{\text{exp}}} + \left[ \frac{\partial N_{\text{H}^0,2}}{\partial t} \right] - A_{2s,1s}^{2q} N_{\text{H}^0,2s} \\ & - k_5 N_{\text{H}^0} N_{\text{H}^0,2s} - k_6 N_{\text{H}^0} N_{\text{H}^0,2p} \\ & - k_8 N_{\text{H}^0,1} N_{\text{H}^0,2s} - k_9 N_{\text{H}^0,1} N_{\text{H}^0,2p} \\ & - k_{14} N_{\text{H}_2} N_{\text{H}^0,2}, \end{aligned} \quad (13)$$

where  $N_{\text{H}^0,2s} = 0.25 N_{\text{H}^0,2}$  and  $N_{\text{H}^0,2p} = 0.75 N_{\text{H}^0,2}$  are the number densities of hydrogen levels 2s and 2p calculated assuming only collisional transition between these states;  $N_{\text{H}^0} = \sum_{k=1}^{15} N_{\text{H}^0,k}$  is the number density of neutral hydrogen;  $N_{\text{H}_2}$  is the number density of  $\text{H}_2$ ;  $A_{2s,1s}^{2q}$  is the probability of the hydrogen two-photon decay;  $k_5$ ,  $k_6$ ,  $k_8$ ,  $k_9$ , and  $k_{14}$  are the rate coefficients for the corresponding reactions from Table B.1. The rate equations for the number density of neutral hydrogen in level 3 and higher levels  $k > 3$  are

$$\begin{aligned} \frac{\partial N_{\text{H}^0,3}}{\partial t} = & -\frac{N_{\text{H}^0,3}}{t_{\text{exp}}} + \left[ \frac{\partial N_{\text{H}^0,3}}{\partial t} \right] - k_7 N_{\text{H}^0} N_{\text{H}^0,3} \\ & - k_{14} N_{\text{H}_2} N_{\text{H}^0,3} \end{aligned} \quad (14)$$

and

$$\frac{\partial N_{\text{H}^0,k}}{\partial t} = -\frac{N_{\text{H}^0,k}}{t_{\text{exp}}} + \left[ \frac{\partial N_{\text{H}^0,k}}{\partial t} \right] - k_{14} N_{\text{H}_2} N_{\text{H}^0,k}, \quad (15)$$

respectively. Similarly, the rate equation for the number density  $N_{z^+,k}$  of ions  $z^+ = \text{Mg}^+, \text{Fe}^+, \text{Ba}^+$  in level  $k$  simply is

$$\frac{\partial N_{z^+,k}}{\partial t} = -\frac{N_{z^+,k}}{t_{\text{exp}}} + \left[ \frac{\partial N_{z^+,k}}{\partial t} \right]. \quad (16)$$

The rate equations for ionized hydrogen, the negative hydrogen ion and molecular hydrogen  $\text{H}_2$ ,  $\text{H}_2^+$  and  $\text{H}_3^+$  are given in Appendix C.

For the two-state atoms and ions the net rate of transitions, for example, from neutral atom  $z$  into ion  $z^+$  by ionization and recombination processes is given by

$$\begin{aligned} \left[ \frac{\partial N_{z^+}}{\partial t} \right] = & N_{z^0} (P_{z^0} + N_e q_{z^0,c} + R_{z^0,c}^\gamma) \\ & - N_{z^+} N_e (\alpha_{z^0} + N_e q_{c,z^0}). \end{aligned} \quad (17)$$

Using the net rate (17) the rate equations for elements with three ionization stages are easily generalized:

$$\frac{\partial N_{z^+}}{\partial t} = -\frac{N_{z^+}}{t_{\text{exp}}} + \left[ \frac{\partial N_{z^+}}{\partial t} \right] - \left[ \frac{\partial N_{z^{2+}}}{\partial t} \right] \quad (18)$$

and

$$\frac{\partial N_{z^{2+}}}{\partial t} = -\frac{N_{z^{2+}}}{t_{\text{exp}}} + \left[ \frac{\partial N_{z^{2+}}}{\partial t} \right]. \quad (19)$$

In particular, the rate equation for singly ionized oxygen taking account of the charge transfer processes in collisions of  $\text{H}^+$  with  $\text{O}$  and  $\text{O}^+$  with  $\text{H}$  is

$$\begin{aligned} \frac{\partial N_{\text{O}^+}}{\partial t} = & -\frac{N_{\text{O}^+}}{t_{\text{exp}}} + \left[ \frac{\partial N_{\text{O}^+}}{\partial t} \right] - \left[ \frac{\partial N_{\text{O}^{2+}}}{\partial t} \right] \\ & + k_{\text{HO}} N_{\text{H}^+} N_{\text{O}^0} - k_{\text{OH}} N_{\text{O}^+} N_{\text{H}^0}, \end{aligned} \quad (20)$$

where  $N_{\text{H}^+}$  is the number density of ionized hydrogen. The net rate (17) for the ions with a detailed level structure ( $\text{Mg}^+$ ,  $\text{Fe}^+$ , and  $\text{Ba}^+$ ) is calculated including all relevant atomic processes.

To close the system of the above rate Eqs. (13)–(16), (C.1)–(C.5), (18)–(20) we use the particle conservation for hydrogen

$$N_{\text{H}^0} + N_{\text{H}^+} + N_{\text{H}^-} + 2N_{\text{H}_2} + 2N_{\text{H}_2^+} + 3N_{\text{H}_3^+} = \frac{\rho X_{\text{H}}}{m_u A_{\text{H}}} \quad (21)$$

and for other elements from He to Ba with three ionization stages

$$N_{z^0} + N_{z^+} + N_{z^{2+}} = \frac{\rho X_z}{m_u A_z}, \quad (22)$$

and the charge conservation

$$N_{\text{H}^+} - N_{\text{H}^-} + N_{\text{H}_2^+} + N_{\text{H}_3^+} + \sum_{z=\text{He}}^{\text{Ba}} (N_{z^+} + 2N_{z^{2+}}) = N_e, \quad (23)$$

where  $X_z$  is the mass fraction of element  $z$ , and  $A_z$  is its atomic weight.

### 3.6. Gas energy equation

The equation of state of a perfect gas can be written as

$$P_g = (N_t + N_e) k T_e, \quad (24)$$

where  $P_g$  is gas pressure and  $N_t$  is the total number density of atoms, molecules and ions of all types. The specific internal energy of particles (per gram) is the sum of the translational, excitation and ionization energies:

$$E_g = \frac{3}{2} \frac{N_t + N_e}{\rho} k T_e + E_{\text{exc}} + E_{\text{ion}}, \quad (25)$$

where

$$E_{\text{exc}} = \sum_{z=\text{H}}^{\text{Ba}^+} \sum_{k>1} \epsilon_{z,k} N_{z,k} \quad (26)$$

is the excitation energy and

$$\begin{aligned} E_{\text{ion}} = & I_{\text{H}} N_{\text{H}^+} - I_{\text{H}^-} N_{\text{H}^-} + I_{\text{H}_2} N_{\text{H}_2^+} + I_{\text{H}_3} N_{\text{H}_3^+} \\ & + \sum_{z=\text{He}}^{\text{Ba}} [I_{z^0} N_{z^0} + (I_{z^0} + I_{z^+}) N_{z^{2+}}], \end{aligned} \quad (27)$$

is the ionization energy. Here  $\epsilon_{z,k}$  is the excitation energy of state  $k$  for the corresponding atoms and ions, and  $I_{\text{H}}$ ,  $I_{\text{H}^-}$ ,  $I_{\text{H}_2}$ ,  $I_{\text{H}_3}$ ,  $I_{z^0}$ ,  $I_{z^+}$  are the ionization potentials of the corresponding atoms, molecules and ions.

The gas energy equation, the first law of thermodynamics for the material, including radiative losses in continuum and lines, the Compton cooling, and non-thermal heating thus reads

$$\begin{aligned} \frac{\partial E_g}{\partial t} + P_g \frac{\partial}{\partial t} \left( \frac{1}{\rho} \right) = & \frac{4\pi}{\rho} \int_0^\infty (\kappa_\nu J_\nu - \eta_\nu^t - \eta_\nu^{2q}) d\nu \\ & - \frac{4\pi}{\rho} \left( \sum_{z=\text{H}}^{\text{Ba}^+} \sum_{l,u} \eta_{ul} + \eta^{\text{C}} \right) + \epsilon^\gamma, \end{aligned} \quad (28)$$

where

$$\eta^C = \frac{4kT_e}{m_e c^2} \sigma_e N_e J \left( 1 - \frac{T_r}{T_e} \right) \quad (29)$$

is the net emissivity of the Compton cooling (Weymann 1966). Here  $\kappa_\nu$  and  $\eta_\nu^t$  are the monochromatic true absorption coefficient corrected for stimulated emission and the monochromatic thermal emissivity, including bound-free and free-free processes for all atoms and ions (Mihalas 1978);  $\eta_\nu^{2q}$  is the two-photon emissivity of hydrogen;  $\eta_{ul}$  is the net frequency-averaged emissivity of line (10);  $\varepsilon^\gamma$  is the rate of energy deposition from the radioactive decays;  $\sigma_e$  is the Thomson scattering cross section;  $J$  is the integrated mean intensity of continuum;  $T_r = (\pi J / \sigma_R)^{1/4}$  is the radiation temperature and  $\sigma_R$  is the Stefan-Boltzmann constant. The energy equation determines the electron temperature in the SN atmosphere which is the same for neutrals and ions.

### 3.7. Computational method

A hydrodynamic model with 300 mass zones provides the velocity  $v(r, t)$  and density  $\rho(r, t)$  profiles, the photospheric radius  $R_{ph}(t)$  and effective temperature  $T_{eff}(t)$ . The simplified description of the continuum radiation field as diluted photospheric radiation permits us to solve for a given mass zone the rate Eqs. (13)–(16), (C.1)–(C.5), (18)–(20), the particle conservation Eqs. (21), (22), the charge conservation Eq. (23), and the gas energy Eq. (28) independently of other mass zones.

As the supernova envelope expands, the photosphere moves inwards. In a steady state the physical values in the atmosphere at certain moment  $t$  are determined by the instant density and radiation field. In a time-dependent approach one has to start from a moment  $t_{ph}$  at which a given mass zone crosses the photosphere, and then to follow the time evolution until  $t$ . To obtain the distribution of physical values in the atmosphere this procedure should be applied to each mass zone.

The simultaneous solution of the above Eqs. (13)–(15), (C.1)–(C.5), (18)–(23), (28) is achieved by reducing them to a system of ordinary differential equations. In particular, the gas energy Eq. (28) is reduced to the ordinary differential equation for electron temperature  $T_e$ . To properly formulate the problem of time evolution of physical values for a given mass zone, initial data must be specified at the photospheric level. This is done by solving the Eqs. (13)–(15), (C.1)–(C.5), (18)–(23) at the photospheric level assuming steady state for a given electron temperature  $T_e$ . This is the simplest way to model the non-equilibrium conditions at the SN photosphere. The derived system of ordinary differential equations is stiff and is integrated by the implicit method of Gear (1971) with an automatic choice of both the time integration step and the order of accuracy of the method.

The recovered time-dependent structure of the atmosphere is used then to calculate spectra at selected epochs. The spectra are modelled by the Monte Carlo technique with relativistic effects included (Mihalas 1978; Jeffery 1993, 1995). We suggest that the photosphere diffusively reflects the incident photons (Chugai & Utrobin 2000). The line scattering is generally non-conservative and is described in terms of the line scattering

albedo. The Thomson scattering on free electrons and Rayleigh scattering on neutral hydrogen are taken into account.

## 4. Results

### 4.1. Early H $\alpha$ and the hydrodynamic model

Preliminary modelling of H $\alpha$  has revealed that at the early epoch the H $\alpha$  line strength was sensitive to the density of the outer layers. A similar sensitivity of the H $\alpha$  strength to the density was found in the steady-state model (Eastman & Kirshner 1989). We use therefore the H $\alpha$  on day 4.64 to constrain the kinetic energy of the hydrodynamic model.

Assuming the initial electron temperature equal to the effective temperature  $T_e = T_{eff}$  we solved the system of rate and energy equations and then computed H $\alpha$  profile for the low-energy model, i.e., for the model N with the kinetic energy  $E = 10^{51}$  erg (Utrobin 2004). The corresponding bolometric light curve and the calculated H $\alpha$  profile on day 4.64 are shown in Figs. 2a and 2b. The computed H $\alpha$  line has too weak absorption at high velocities compared to the observations (Phillips et al. 1988). The situation, however, is markedly improved for the high-energy model with  $E = 1.5 \times 10^{51}$  erg (Figs. 2c and 2d). The greater strength of the H $\alpha$  absorption in the high-energy model is the direct outcome of the higher density in the outer layers. Thus, the strength of the H $\alpha$  absorption at high velocities indicates the energy-to-mass ratio  $E/M \approx 0.83 \times 10^{50}$  erg  $M_\odot^{-1}$ . We adopt the model with high energy as the standard model for our computations of the SN 1987A atmosphere.

### 4.2. Evolution of hydrogen ionization and H $\alpha$

With the adopted photospheric continuum and the initial electron temperature we are able to compute for given moments the distribution of the essential physical values in the atmosphere, including the hydrogen level populations. The initial electron temperature at the photosphere is adopted equal to the effective temperature  $T_{eff}$  which is taken from the hydrodynamical calculations (Utrobin 2004).

#### 4.2.1. Day 4.64

On day 4.64 the H $\alpha$  profile computed in the time-dependent model A fits the observed one fairly well (Fig. 3a), while model B underproduces the emission component (Fig. 3b). This suggests that the average intensity of the UV radiation in the atmosphere at this and earlier epochs is closer to that of model A. Yet the H $\alpha$  absorption is apparently weak in the blue wing in model A. This is partially due to the higher rate of the hydrogen photoionization from the second level for the adopted black-body Balmer continuum in this case (Fig. 1). Both A and B steady-state models predict extremely weak H $\alpha$  line. This reflects the fact that the steady-state ionization is significantly lower than that in the time-dependent model, while the electron temperature is too low for the collisional excitation. This situation persists during all the period studied.

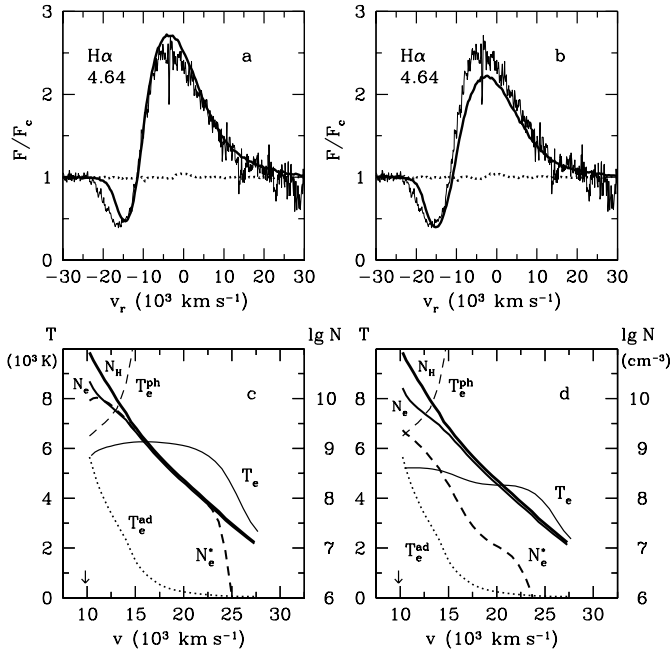


**Fig. 3.**  $H\alpha$  line profile and the structure of the atmosphere on day 4.64. Panel a):  $H\alpha$  profile, computed with the time-dependent model A (thick solid line) and with the steady-state model A (dotted line), is overplotted on the observed profile obtained by Phillips et al. (1988) (thin solid line). Panel b): the same as panel a) but for model B. Panel c): the calculated hydrogen number density (thick solid line), electron number density (medium solid line) and electron temperature (thin solid line) in the time-dependent model A. The medium dashed line gives the equilibrium electron number density calculated for  $T = T_e$ . The thin dashed line shows the initial electron temperature  $T_e^{\text{ph}}$  at the photosphere as a function of velocity, while the dotted line is the distribution of the electron temperature  $T_e^{\text{ad}}$  evaluated with the purely adiabatic cooling. Arrow indicates the photospheric level. Panel d): the same as panel c) but for model B.

As expected, the electron temperature in model A is larger than in model B since the radiative heating rate in model A with the black-body UV continuum is higher than in model B (Figs. 3c and 3d). The remarkable property of the distribution of electron temperature in the atmosphere for both models is a fast drop from the initial value at the photosphere of  $T_{\text{eff}}$  to  $\sim(0.75-0.80) T_{\text{eff}}$ . This drop results from the fact that the electron temperature calculated in the diluted radiation field is lower than the effective temperature. The same physics leads to the well-known relation for the boundary temperature of a gray atmosphere  $T_0 \approx 0.81 T_{\text{eff}}$  (see, e.g., Mihalas 1978).

Despite the relatively high electron temperature in the atmosphere, the electron concentration in the time-dependent model essentially exceeds the equilibrium value  $N_e^*$  predicted by the Saha equation for  $T = T_e$ . The difference is obviously greater for the model B with lower  $T_e$  (Figs. 3c and 3d).

Although the electron temperature is relatively high in the most of the atmosphere,  $T_e > 4000$  K, (Figs. 3c and 3d) it is insufficient to maintain the large optical depth of  $H\alpha$  demonstrated by the time-dependent models. The primary mechanism of the population of the second level is the recombination to excited levels.

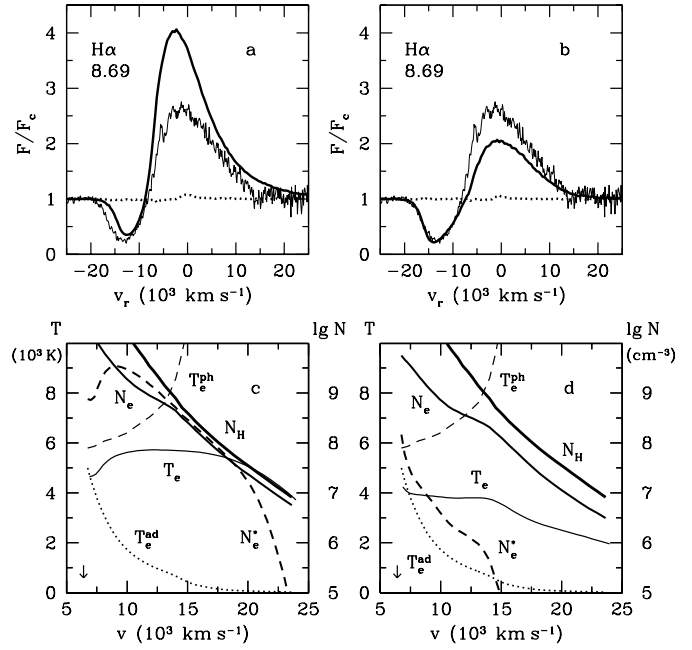


**Fig. 4.**  $H\alpha$  line profile and the structure of the atmosphere on day 8.69. See Fig. 3 legend for details.

Noteworthy, the populations of excited levels are small numbers that are controlled by the relatively fast transition rates. As a result the relaxation times for the level populations of hydrogen are short:  $N_{H^0,k}/(dN_{H^0,k}/dt) \ll t$ . We conclude, therefore, that the population of the second hydrogen level, and the  $H\alpha$  optical depth as well, is determined mainly by the current values of the electron concentration and the photoionization rates, although  $N_e$  is essentially a time-dependent value. The same arguments are valid for the level populations and ionization of metals: they may be calculated using the steady-state approximation on the background of the time-dependent electron concentration and temperature.

#### 4.2.2. Day 8.69

On day 8.69 the both A and B models satisfactorily reproduce the absorption component of  $H\alpha$  (Figs. 4a and 4b). The strength of the observed emission lies between the two models which implies that the actual radiation field in the UV band is intermediate between A and B cases.

The electron concentration shows a kink at about  $14000 \text{ km s}^{-1}$  (Figs. 4c and 4d) that was only barely seen at the previous date (Figs. 3c and 3d). The position of this kink correlates with the transition from the full ionization to partial ionization at the photosphere that occurred after  $t \approx 2$  days and was imprinted on the ionization pattern on day 4.64 as well (Fig. 3d).

#### 4.2.3. Day 14.68 and 19.68

We found that the  $H\alpha$  emission in the model A for  $t \geq 8$  days has tremendous and progressively growing intensity, in apparent contradiction with observations. This reflects the

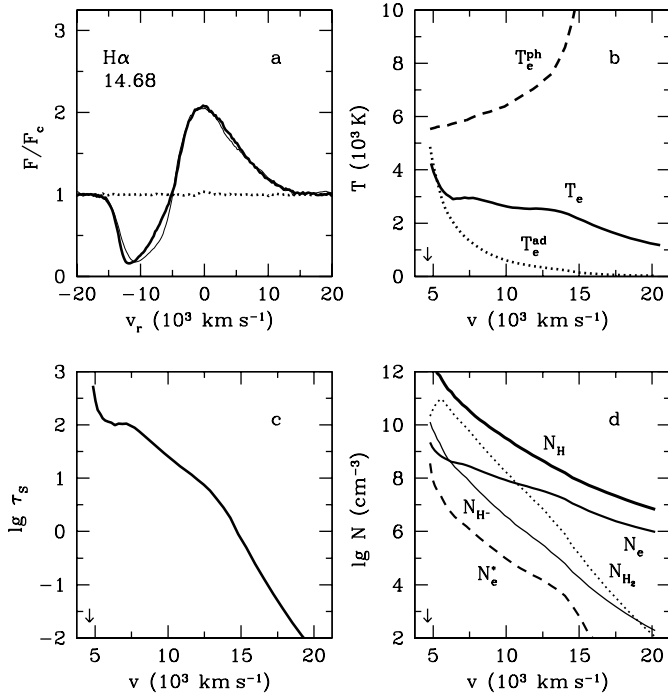


**Fig. 5.**  $H\alpha$  line profile and the structure of the atmosphere on day 14.68. Panel **a**):  $H\alpha$  profile, computed with the time-dependent model B (*thick solid line*) and with the steady-state model B (*dotted line*), is overplotted on the observed profile obtained by Hanuschik & Dachs (1988) (*thin solid line*). Panel **b**): the calculated electron temperature (*solid line*) in the time-dependent model B. The *dashed line* shows the initial electron temperature  $T_e^{\text{ph}}$  at the photosphere as a function of velocity, while the *dotted line* is the distribution of the electron temperature  $T_e^{\text{ad}}$  evaluated with purely adiabatic cooling. Panel **c**): the Sobolev optical depth of  $H\alpha$  as a function of velocity. Panel **d**): the calculated hydrogen number density  $N_{\text{H}}$  (*thick solid line*), electron number density  $N_{\text{e}}$  (*medium solid line*), number density of negative hydrogen ion  $N_{\text{H}^-}$  (*thin solid line*), and number density of molecular hydrogen  $N_{\text{H}_2}$  (*dotted line*) in the time-dependent model B. The *dashed line* gives the equilibrium electron number density  $N_{\text{e}}^*$  calculated for  $T = T_{\text{e}}$ . The number densities of negative hydrogen ion and molecular hydrogen are shifted by +9 dex and +4 dex, respectively. Arrow indicates the photospheric level.

increasing disparity between the black-body assumption and the real behavior of the UV continuum (Fig. 1). We exclude, therefore, model A from further analysis as irrelevant and focus, instead, on model B as most adequate for the later stages. The calculated  $H\alpha$  profile in the model B on day 14.68 (Fig. 5a) and 19.68 (Fig. 6a) fit the observed profile fairly well which confirms that around these epochs the UV continuum radiation adopted in this model is close to the reality.

The electron temperature in the most of the atmosphere on day 14.68 is  $\sim 3000$  K and  $\sim 2000$  K on day 19.68. The adiabatic cooling dominates in model B at the low velocities as indicated by the close run of temperatures  $T_{\text{e}}$  and  $T_{\text{e}}^{\text{ad}}$  (Figs. 5b and 6b). This behavior of electron temperature emphasizes the time-dependent nature of the gas energy balance. Note that the formal addition of the adiabatic cooling term to the steady-state gas energy equation would not produce the above result.

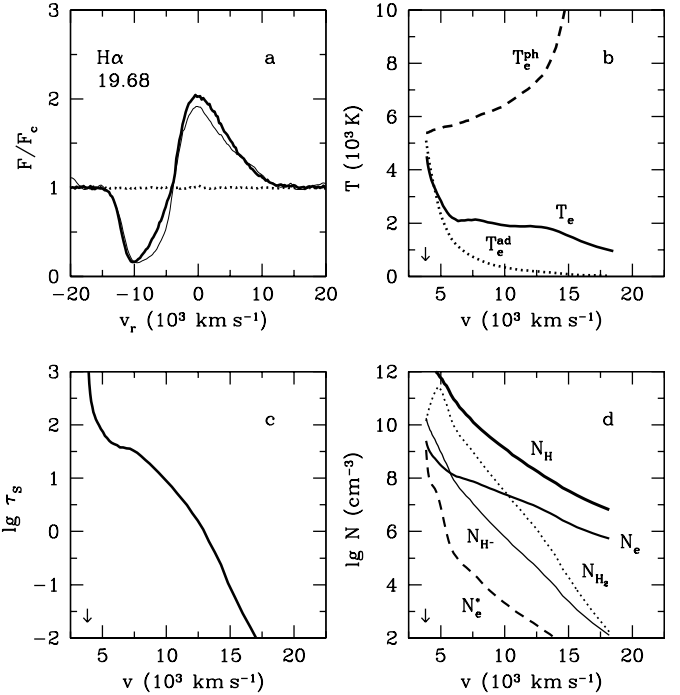


**Fig. 6.**  $H\alpha$  line profile and the structure of the atmosphere on day 19.68. See Fig. 5 legend for details.

Figures 5d, 6d and 7d show the behavior of concentrations of the  $\text{H}^-$  and  $\text{H}_2$  molecules on day 14.68, 19.68 and 29.68, respectively. The hydrogen neutralization via the chain  $\text{H}_2 + \text{H}^+ \rightarrow \text{H}_2^+ + \text{H}$  and  $\text{H}_2^+ + \text{e} \rightarrow 2\text{H}$  may be important for certain parameters of SN 1987A (Utrobin & Chugai 2002). However, for the present model B the effect of the hydrogen neutralization is small (though not negligible) compared to the hydrogen recombination.

#### 4.2.4. Day 29.68

On day 29.68 the model B fits the observed profile quite well, while in the steady-state model the  $H\alpha$  line remains extremely weak (Fig. 7a). Remarkably, the time-dependent model reproduces the strength of the  $H\alpha$  line in the whole range of the radial velocities. This implies that the admixed  $^{56}\text{Ni}$  in the outer layers is not needed to account for the strong  $H\alpha$  line in SN 1987A at the age of  $t \leq 30$  days.

Between day 20 and 29 the additional blue and red peaks emerge in the observed  $H\alpha$  profile, a phenomenon known as the “Bochum event” (Hanuschik & Dachs 1988). We believe that the red peak is related to the high velocity  $^{56}\text{Ni}$  clump in the far hemisphere, whereas the blue peak reflects a minimum in the spherically-symmetric radial distribution of the  $H\alpha$  optical depth at  $\approx 5000$   $\text{km s}^{-1}$  (Chugai 1991b; Utrobin et al. 1995). Although our model B shows a steep drop of the  $H\alpha$  optical depth outside the photosphere by more than three orders of magnitudes (Fig. 7c), the drop is not sufficient to produce the minimum of  $\tau_{\text{S}}$  at  $5000$   $\text{km s}^{-1}$ .

Interestingly, the concentration of the hydrogen molecule  $\text{H}_2$  shows a non-monotonic behavior with the maximum at about  $3800$   $\text{km s}^{-1}$ , which coincides with the



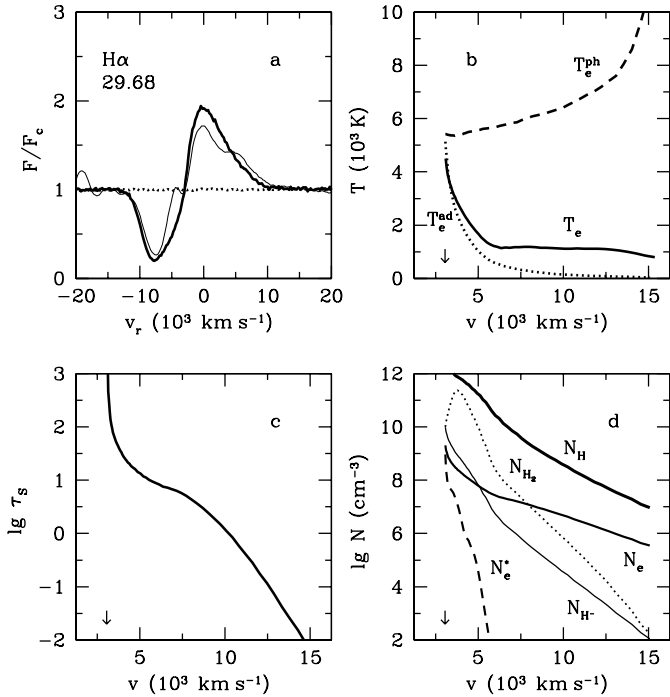


**Fig. 7.**  $H\alpha$  line profile and the structure of the atmosphere on day 29.68. See Fig. 5 legend for details.

required minimum of the  $H\alpha$  optical depth. We estimated that a slight increase of the electron temperature is able to make hydrogen neutralization  $H_2 + H^+ \rightarrow H_2^+ + H$  and  $H_2^+ + e \rightarrow 2H$  competitive with hydrogen recombination at the maximum of  $H_2$  concentration. Therefore, the hydrogen neutralization at  $\sim 3800 \text{ km s}^{-1}$ , and the formation of the local minimum of the  $H\alpha$  optical depth remains an exciting possibility (Utrobin & Chugai 2002). The final answer, however, requires a more refined model that in addition to time-dependent effects must correctly treat radiation transfer.

#### 4.3. Barium problem

The unusually strong Ba II 6142 Å line in early spectra of SN 1987A is a distinctive feature of this supernova (Williams 1987). The “Ba problem” is the disparity between the high Ba overabundance factor  $\zeta = (\text{Ba}/\text{Fe})_{87A}/(\text{Ba}/\text{Fe})_{\text{LMC}} \sim 5$  derived from Ba II 6142 Å line (Mazzali et al. 1992) and the theoretical predictions of  $s$ -process calculations. The  $s$ -process nucleosynthesis in the massive stars evolving to the presupernova star of SN 1987A (Prantzos et al. 1990) yields the Ba overabundance of  $\zeta \sim 1.3$ –1.4 in the hydrogen-rich envelope, assuming that a total ejecta mass is 15–18  $M_{\odot}$ , a mass-cut is at 2  $M_{\odot}$  (Woosley & Weaver 1995), and the synthesized Ba is completely mixed over the ejecta. In fact, it is difficult to imagine that Ba produced at the He-burning stage can be significantly mixed with the hydrogen envelope. More realistic would be a situation with the LMC abundance of Ba in the hydrogen envelope. Given the problem with  $H\alpha$  description in all the steady-state models, we revisit the issue of Ba in SN 1987A on the basis of our time-dependent approach.

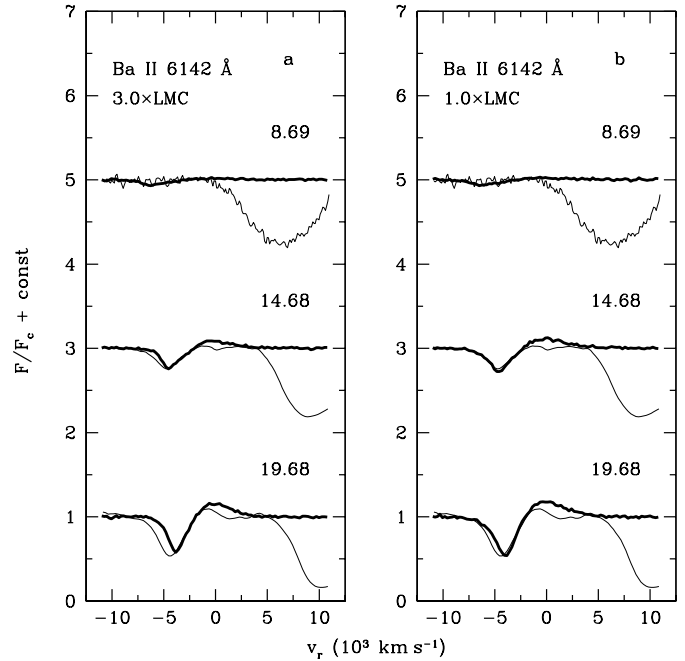


**Fig. 8.** Evolution of Ba II 6142 Å line from day 8.69 till 19.68 in SN 1987A. The Ba II 6142 Å profiles, computed with the time-dependent model B (*thick solid line*), are overlotted on those observed by Phillips et al. (1988) and Hanuschik & Dachs (1988) (*thin solid line*). *Left panel a*): models for the relative Ba overabundance of 3.0. *Right panel b*): models for the relative Ba overabundance of 1.0 and with the suppressed far UV continuum.

We compute the Ba ionization and excitation, using the multilevel Ba II model described in Appendix A.4, with the continuum model B for the two choices of the far UV ( $10.0 < h\nu < 13.6 \text{ eV}$ ) radiation in the SN envelope. In the first version, the continuum in this energy range is described by the solution of Chandrasekhar (1934), our standard assumption. In the second version we follow the suggestion of Mazzali et al. (1992) that the far UV continuum is essentially suppressed by the line-blocking (in fact Rayleigh scattering also contributed to the blocking effect). This assumption essentially increases the ionization fraction of Ba II and thus decreases the overabundance factor. However, we modify this assumption making it more realistic: we adopt that the far UV ( $10.0 < h\nu < 13.6 \text{ eV}$ ) radiation is in equilibrium with matter and is characterized by the local electron temperature of our time-dependent model. Unfortunately, the IUE observations cannot provide a confident verification of our assumption about the far UV flux in SN 1987A because of the dominant contribution of the light from stars 2 and 3 to this band (Pun et al. 1995). The accepted suppression of the far UV continuum does not affect the computed  $H\alpha$  line at all.

The Ba II 6142 Å line profile calculated for three phases preceding the Bochum event are shown in Fig. 8. In the first version of the UV continuum (model B and Chandrasekhar approximation for the average intensity) the required Ba overabundance is at least  $\zeta = 3.0$  (Fig. 8a). In the second case (suppressed far UV continuum) the Ba II 6142 Å line is reproduced for the LMC abundance of Ba ( $\zeta = 1$ ) (Fig. 8b). We thus

conclude that the model B with the suppressed far UV radiation, adopted also by Mazzali et al. (1992), recovers the LMC abundance of Ba from the Ba II 6142 Å line strength.

At present, there is no reason to claim that the Ba in the hydrogen-rich envelope of SN 1987A is markedly overabundant. The “Ba problem” in SN 1987A, in our opinion, has appeared as a by-product of the assumption of the steady-state hydrogen ionization.

## 5. Discussion and conclusions

Our goal has been to explore the role of time-dependent effects in the ionization and excitation of hydrogen in the atmosphere of SN 1987A. We have developed a model that computes the time-dependent kinetics of relevant processes together with the time-dependent energy balance. The computations have confirmed our previous conclusion (Utrobin & Chugai 2002) that the effect of the time-dependent ionization in SN 1987A at the photospheric epoch is strong: the hydrogen ionization in the atmosphere is significantly higher than in steady-state approach and, as a result, the hydrogen excitation is higher as well. In addition we have found that the temperature structure in the atmosphere is essentially determined by time-dependent effects of the gas energy balance. The H $\alpha$  formation at the photospheric epoch during the first month is primarily controlled by the time-dependent ionization effect and additional excitation by the external  $^{56}\text{Ni}$  is not needed to account for the strength of the H $\alpha$  line.

We have failed to reproduce the additional blue peak in the H $\alpha$  line (Bochum event) that emerges between day 20 and 29 (Hanuschik & Dachs 1988). Yet we still believe that the blue peak is the result of the non-monotonic behavior of the hydrogen concentration on the second level ( $N_2$ ). Remarkably, the H $_2$  concentration reveals the non-monotonic behavior with the maximum of H $_2$  number density around 3800 km s $^{-1}$  on day 29. In this regard we do not rule out that a more accurate treatment of the UV radiation transfer may reveal the major role of molecular processes in creating the non-monotonic behavior of the  $N_2$  number density as suggested earlier (Utrobin & Chugai 2002).

In the epoch preceding the Bochum event the time-dependent model produces a realistic distribution of the hydrogen fractional ionization in the atmosphere. With this structure we are able to reproduce the Ba II 6142 Å line in SN 1987A on day 14.68 and 19.68 with the LMC abundance of Ba. We believe, therefore, that the Ba problem, i.e., unacceptably high Ba overabundance in SN 1987A, is resolved. The missing physics of the former models is identified: the time-dependent hydrogen ionization that provides a higher electron concentration in the atmosphere and thus more efficient recombination of Ba III into Ba II compared to the steady-state approximation.

*Acknowledgements.* V.P.U. is grateful to Wolfgang Hillebrandt and Ewald Müller for hospitality during stay at the MPA, and also would like to thank Manuel Bautista and Keith Butler for kindly providing him with the photoionization cross sections of singly ionized iron and barium, respectively. N.N.C. thanks Roger Chevalier for hospitality at Department of Astronomy of the University of Virginia, where a part of this work has been done. Our special thanks to the referee

Leon Lucy whose comments and suggestions have stimulated improvement of the manuscript. This work has been supported in part by the Russian Foundation for Fundamental Research (04-01-17255).

## References

- Abel, T., Anninos, P., Zhang, Y., & Norman, M. L. 1997, *New Astron.*, 2, 181
- Aggarwal, K. M., Berrington, K. A., Burke, P. G., Kingston, A. E., & Pathak, A. 1991, *J. Phys. B: Atom. Molec. Opt. Phys.*, 24, 1385
- Allen, C. W. 1973, *Astrophysical Quantities* (London: Athlone Press)
- Bautista, M. A., & Pradhan, A. K. 1998, *ApJ*, 492, 650
- Bautista, M. A., Romano, P., & Pradhan, A. K. 1998, *ApJS*, 118, 259
- Bell, K. L., & Berrington, K. A. 1987, *J. Phys. B: Atom. Molec. Phys.*, 20, 801
- Butler, K. 2000, private communication
- Callaway, J. 1994, *At. Data Nucl. Data Tables*, 57, 9
- Castor, J. I. 1970, *MNRAS*, 149, 111
- Catchpole, R. M., Menzies, J. M., Monk, A. S., et al. 1987, *MNRAS*, 229, 15P
- Catchpole, R. M., Whitelock, P. A., Feast, M. W., et al. 1988, *MNRAS*, 231, 75P
- Chandrasekhar, S. 1934, *MNRAS*, 94, 444
- Chugai, N. N. 1980, *SvAL*, 6, 91
- Chugai, N. N. 1991a, in *Supernovae*, ed. S. E. Woosley (New York: Springer-Verlag), 286
- Chugai, N. N. 1991b, *SvAL*, 17, 400
- Chugai, N. N. 1998, *Astron. Lett.*, 24, 632
- Chugai, N. N., & Utrobin, V. P. 2000, *A&A*, 354, 557
- Clayton, D. D., Leising, M. D., The, L.-S., Johnson, W. N., & Kurfess, J. D. 1992, *ApJ*, 399, L141
- Culhane, M., & McCray, R. 1995, *ApJ*, 455, 335
- Cunto, W., Mendoza, C., Ochsenein, F., & Zeippen, C. J. 1993, *A&A*, 275, L5
- Dufour, R. J. 1984, in *Structure and Evolution of the Magellanic Clouds*, ed. S. van den Bergh, & K. S. de Boer (Dordrecht: Reidel), IAU Symp., 108, 353
- Eastman, R. G., & Kirshner, R. P. 1989, *ApJ*, 347, 771
- Fransson, C., & Kozma, C. 1993, *ApJ*, 408, L25
- Fuller, T. M., & Couchman, H. M. P. 2000, *ApJ*, 544, 6
- Galli, D., & Palla, F. 1998, *A&A*, 335, 403
- Gear, C. W. 1971, *Numerical initial value problems in ordinary differential equations* (New Jersey: Prentice-Hall)
- Giovanardi, C., Natta, A., & Palla, F. 1987, *A&AS*, 70, 269
- Hamuy, M., Suntzeff, N. B., Gonzalez, R., & Martin, G. 1988, *AJ*, 95, 63
- Hanuschik, R. W., & Dachs, J. 1988, *A&A*, 205, 135
- Hollenbach, D. J., & McKee, C. F. 1989, *ApJ*, 342, 306
- Irwin, A. W. 1981, *ApJS*, 45, 621
- Jeffery, D. J. 1993, *ApJ*, 415, 734
- Jeffery, D. J. 1995, *ApJ*, 440, 810
- Johansson, S., & Jordan, C. 1984, *MNRAS*, 210, 239
- Johnson, L. C. 1972, *ApJ*, 174, 227
- Karzas, W. J., & Latter, R. 1961, *ApJS*, 6, 167
- Kirshner, R. P., & Kwan, J. 1975, *ApJ*, 197, 415
- Kozma, C., & Fransson, C. 1992, *ApJ*, 390, 602
- Kurucz, R. L., & Bell, B. 1995, *Atomic Line Data*, Kurucz CD-ROM No. 23 (Cambridge, Mass.: Smithsonian Astrophysical Observatory)
- Latter, W. B., & Black, J. H. 1991, *ApJ*, 372, 161
- Li, H., McCray, R., & Sunyaev, R. A. 1993, *ApJ*, 419, 824
- Lotz, W. 1969, *Zs. Physik*, 220, 466
- Lundqvist, P., & Fransson, C. 1996, *ApJ*, 464, 924

- Mazzali, P. A., Lucy, L. B., & Butler, K. 1992, *A&A*, 258, 399
- Meaburn, J., Bryce, M., & Holloway, A. J. 1995, *A&A*, 299, L1
- Michael, E., McCray, R., Chevalier, R., et al. 2003, *ApJ*, 593, 809
- Mihalas, D. 1978, *Stellar Atmospheres* (San-Francisco: Freeman)
- Milkey, R. W., & Mihalas, D. 1974, *ApJ*, 192, 769
- Nahar, S. N., & Pradhan, A. K. 1994, *Phys. Rev. A*, 49, 1816
- Nussbaumer, H., & Schmutz, W. 1984, *A&A*, 138, 495
- Palla, F., Salpeter, E. E., & Stahler, S. W. 1983, *ApJ*, 271, 632
- Phillips, M. M., Heathcote, S. R., Hamuy, M., & Navarrete, M. 1988, *AJ*, 95, 1087
- Prantzos, N., Hashimoto, M., & Nomoto, K. 1990, *A&A*, 234, 211
- Pun, C. S. J., Kirshner, R. P., Sonneborn, G., et al. 1995, *ApJS*, 99, 223
- Rawlings, J. M. C. 1988, *MNRAS*, 232, 507
- Rawlings, J. M. C., Drew, J. E., & Barlow, M. J. 1993, *MNRAS*, 265, 968
- Roberge, W., & Dalgarno, A. 1982, *ApJ*, 225, 176
- Scholz, T. T., Walters, H. R. J., Burke, P. G., & Scott, M. P. 1990, *MNRAS*, 242, 692
- Schöning, T., & Butler, K. 1998, *A&AS*, 128, 581
- Shapiro, P. R., & Kang, H. 1987, *ApJ*, 318, 32
- Sigut, T. A. A., & Pradhan, A. K. 1995, *J. Phys. B: Atom. Molec. Phys.*, 28, 4879
- Sobelman, I. I., Vainshtein, L. A., & Yukov, E. A. 1981, *Excitation of Atoms and Broadening of Spectral Lines*, Springer Ser. Chem. Phys. 7 (Berlin: Springer)
- Sobolev, V. V. 1960, *Moving Envelopes of Stars* (Cambridge: Harvard University Press)
- Stancil, P. C. 1994, *ApJ*, 430, 360
- Stancil, P. C., Schultz, D. R., Kimura, M., et al. 1999, *A&AS*, 140, 225
- Stibbe, D. T., & Tennyson, J. 1999, *ApJ*, 513, L147
- Sutherland, R. S. 1998, *MNRAS*, 300, 321
- Sutherland, R. S., & Dopita, M. A. 1993, *ApJS*, 88, 253
- Utrobin, V. P. 2004, *Astron. Lett.*, 30, 293
- Utrobin, V. P., & Chugai, N. N. 2002, *Astron. Lett.*, 28, 386
- Utrobin, V. P., Chugai, N. N., & Andronova, A. A. 1995, *A&A*, 295, 129
- Van Regemorter, H. 1962, *ApJ*, 136, 906
- Verner, D. A., & Yakovlev, D. G. 1995, *A&AS*, 109, 125
- Verner, D. A., Ferland, G. J., Korista, K. T., & Yakovlev, D. G. 1996, *ApJ*, 465, 487
- Voronov, G. S. 1997, *At. Data Nucl. Data Tables*, 65, 1
- Wang, L. 1991, *A&A*, 246, L69
- Weymann, R. 1966, *ApJ*, 145, 560
- Wiese, W. L., Smith, M. W., & Glennon, B. M. 1966, *Atomic Transition Probabilities. Volume I. Hydrogen Through Neon (NSRDS-NBS 4)*
- Williams, R. E. 1987, *ApJ*, 320, L117
- Wishart, A. W. 1979, *MNRAS*, 187, 59P
- Woosley, S. E., & Weaver, T. A. 1995, *ApJS*, 101, 181
- Woosley, S. E., Heger, A., Weaver, T. A., & Langer, N. 1997, in *SN 1987A: Ten Years Later*, ed. M. M. Phillips, & N. B. Suntzeff, in press
- Yan, M., Sadeghpour, H. R., & Dalgarno, A. 1998, *ApJ*, 496, 1044
- Yan, M., Sadeghpour, H. R., & Dalgarno, A. 2001, *ApJ*, 559, 1194
- Zeldovich, Ya. B., Kurt, V. G., & Sunyaev, R. A. 1968, *JETP*, 55, 278
- Zhang, H. L., & Pradhan, A. K. 1995, *A&A*, 293, 953

# Online Material

## Appendix A: atomic data

### A.1. Hydrogen

For hydrogen we use a model atom consisting of 15 levels, all of them being treated as single levels. The energy levels and oscillator strengths for the all transitions are taken from Wiese et al. (1966). The radiative probability of the hydrogen  $2s-1s$  two-photon transition and the distribution of the hydrogen two-photon continuum are given by Nussbaumer & Schmutz (1984). The photoionization cross sections of hydrogen are computed with the formulae and tables of Karzas & Latter (1961). The temperature-averaged free-free Gaunt factor is interpolated from the table and accurate extrapolations given by Sutherland (1998). The electron collisional excitation and deexcitation rates for atomic hydrogen are calculated with the effective collision strengths taken from Scholz et al. (1990), Callaway (1994), Aggarwal et al. (1991) and Giovanardi et al. (1987). The electron collisional ionization rates for atomic hydrogen are calculated using the approximate formulae of Johnson (1972). The rate coefficients for charge transfer in collisions of  $O^+$  with H and  $H^+$  with O are given by Stancil et al. (1999).

### A.2. Singly ionized magnesium

For singly ionized magnesium we use a model ion consisting of 9 single levels. The energy levels and oscillator strengths for the all transitions are compiled from the Atomic Spectroscopic Database (ASD) at the National Institute of Standards and Technology (NIST) and from Kurucz & Bell (1995). The photoionization cross sections of ionized magnesium are taken from the Opacity Project atomic database (Cunto et al. 1993). The effective collision strengths for the electron excitation of ionized magnesium were computed by Sigut & Pradhan (1995). The electron collisional ionization rates for singly ionized magnesium are evaluated by fits of Voronov (1997), the approximate formula of Milkey & Mihalas (1974), and the semi-empirical formula of Lotz (1969).

### A.3. Singly ionized iron

For the specific case of the Fe II ion a 30-term, multilevel atom model is employed. A total number of 212 transitions between these terms from 2150 Å to 55 μm are calculated. The energy levels and oscillator strengths for the all transitions in singly ionized iron are compiled from ASD at NIST and from Kurucz & Bell (1995). The photoionization cross sections of ionized iron are taken from Nahar & Pradhan (1994) and Bautista & Pradhan (1998), and averaged over resonance structures according to Bautista et al. (1998). The Maxwellian averaged rate coefficients for the infrared, optical and ultraviolet transitions in ionized iron are taken from Zhang & Pradhan (1995). The collision strengths for some transitions are calculated by using an empirical formula derived from the available experimental and theoretical data for Fe II (Li et al. 1993). The rate of direct collisional ionization for singly ionized iron from the ground state is computed using the fits from Voronov (1997)

and the electron collisional ionization rates from excited levels are evaluated by the semi-empirical formula of Lotz (1969).

### A.4. Singly ionized barium

For the case of the Ba II ion a 17-term, multilevel atom model is used with a total number of 56 transitions between these terms from 1500 Å to 58 μm. The energy levels and oscillator strengths for the all transitions in singly ionized barium are taken from Kurucz & Bell (1995). The photoionization cross sections of ionized barium are given by Butler (2000) and averaged over resonance structures according to Bautista et al. (1998). The electron collisional excitation rates for ionized barium are taken from Schöning & Butler (1998) and compiled from Sobelman et al. (1981) and Van Regemorter (1962). The electron collisional ionization rates are evaluated by the semi-empirical formula of Lotz (1969).

### A.5. Other atoms and ions

The following elements are included in the non-steady study: He, C, N, O, Ne, Na, Mg, Si, S, Ar, Ca, Fe and Ba. All elements are treated with the three ionization stages. The atoms and ions are assumed to consist of the ground state and continuum except the singly ionized elements with a detailed energy level structure. Atomic weights and ionization potentials are from Allen (1973). The partition functions are calculated with the polynomial approximation fit obtained by Irwin (1981). The photoionization cross sections of atoms and ions are evaluated with data of Verner & Yakovlev (1995) and Verner et al. (1996). The temperature-averaged free-free Gaunt factor is taken from Sutherland (1998). The free-free absorption coefficient is calculated with the effective nuclear charge including screening effects (Sutherland & Dopita 1993). The electron collisional ionization rates for atoms and ions are computed using the approximate formulae of Voronov (1997).

## Appendix B: molecular data

### B.1. Negative hydrogen ion

The photoionization cross section data for negative hydrogen ion are taken from Wishart (1979). The free-free absorption coefficient of negative hydrogen ion was calculated by Bell & Berrington (1987).

### B.2. Other hydrogen molecules

The neutral-neutral reactions for hydrogen molecules are listed in Table B.1 with their names and references from which the corresponding rate coefficients are taken. Tables B.2 and B.3 list the ion-neutral and ion-ion reactions for hydrogen molecules with the relevant references, respectively. The electron reactions for hydrogen molecules are listed in Table B.4 with their names and references from which the corresponding rate coefficients are taken. Table B.5 gives the photoionization and photodissociation processes, their names, and references from which the photoionization and photodissociation

**Table B.1.** List of neutral-neutral reactions.

No.Reaction	Source
1 $H + H \rightarrow H^+ + H + e^-$	Hollenbach & McKee (1989)
2 $H + H \rightarrow H^+ + H^-$	Hollenbach & McKee (1989)
3 $H + H + H \rightarrow H_2 + H$	Palla et al. (1983)
4 $H + H + H_2 \rightarrow 2H_2$	Palla et al. (1983)
5 $H(2s) + H \rightarrow H_2^+ + e^-$	Rawlings et al. (1993)
6 $H(2p) + H \rightarrow H_2^+ + e^-$	Rawlings et al. (1993)
7 $H(3) + H \rightarrow H_2^+ + e^-$	Rawlings et al. (1993)
8 $H(2s) + H(1s) \rightarrow H_2 + \gamma$	Latter & Black (1991)
9 $H(2p) + H(1s) \rightarrow H_2 + \gamma$	Latter & Black (1991)
10 $H + H_2 \rightarrow 3H$	Roberge & Dalgarno (1982)
11 $H + H_2 \rightarrow H^- + H_2^+$	Hollenbach & McKee (1989)
12 $H + H_2 \rightarrow H_2^+ + H + e^-$	Hollenbach & McKee (1989)
13 $H + H_2 \rightarrow H^+ + H_2 + e^-$	Hollenbach & McKee (1989)
14 $H^+ + H_2 \rightarrow H_3^+ + e^-$	Culhane & McCray (1995)
15 $H_2 + H_2 \rightarrow H_2^+ + H_2 + e^-$	Hollenbach & McKee (1989)
16 $H_2 + H_2 \rightarrow H_2 + 2H$	Rawlings (1988)

**Table B.2.** List of ion-neutral reactions.

No.Reaction	Source
17 $H^- + H \rightarrow 2H + e^-$	Abel et al. (1997)
18 $H^- + H \rightarrow H_2 + e^-$	Galli & Palla (1998)
19 $H^+ + H \rightarrow H_2^+ + \gamma$	Galli & Palla (1998)
20 $H^+ + H_2 \rightarrow H_3^+ + \gamma$	Galli & Palla (1998)
21 $H^+ + H_2 \rightarrow H_2^+ + H$	Galli & Palla (1998)
22 $H_2^+ + H \rightarrow H_2 + H^+$	Galli & Palla (1998)
23 $H_2^+ + H_2 \rightarrow H_3^+ + H$	Hollenbach & McKee (1989)
24 $H_2^+ + H_2 \rightarrow H_2 + H^+ + H$	Hollenbach & McKee (1989)
25 $H_3^+ + H \rightarrow H_2 + H_2^+$	Galli & Palla (1998)
26 $H_3^+ + H_2 \rightarrow H_2 + H_2^+ + H$	Hollenbach & McKee (1989)
27 $H_3^+ + H_2 \rightarrow 2H_2 + H^+$	Hollenbach & McKee (1989)

**Table B.3.** List of ion-ion reactions.

No.Reaction	Source
28 $H^- + H^+ \rightarrow 2H$	Galli & Palla (1998)
29 $H^- + H^+ \rightarrow H_2^+ + e^-$	Galli & Palla (1998)
30 $H^- + H_2^+ \rightarrow H + H_2$	Abel et al. (1997)

cross sections are taken. These cross sections are used in calculating the ionization and dissociation rates in the radiation field presented in Sect. 3.1.

**Table B.4.** List of electron reactions.

No.Reaction	Source
31 $e^- + H^- \rightarrow H + 2e^-$	Abel et al. (1997)
32 $e^- + H_2 \rightarrow 2H + e^-$	Stibbe & Tennyson (1999)
33 $e^- + H_2 \rightarrow H + H^-$	Fuller & Couchman (2000)
34 $e^- + H_2 \rightarrow H_2^+ + 2e^-$	Hollenbach & McKee (1989)
35 $e^- + H_2^+ \rightarrow 2H$	Galli & Palla (1998)
36 $e^- + H_3^+ \rightarrow H + H_2$	Galli & Palla (1998)
37 $e^- + H_3^+ \rightarrow 3H$	Hollenbach & McKee (1989)

**Table B.5.** List of photoionization and photodissociation processes.

No.Process	Source
1 $H_2 + \gamma \rightarrow H_2^+ + e^-$	Yan et al. (1998, 2001)
2 $H_2 + \gamma \rightarrow 2H$	Abel et al. (1997)
3 $H_2 + \gamma \rightarrow H_2^* \rightarrow 2H$	Abel et al. (1997)
4 $H_2^+ + \gamma \rightarrow H + H^+$	Stancil (1994)
5 $H_2^+ + \gamma \rightarrow 2H^+ + e^-$	Shapiro & Kang (1987)

### Appendix C: rate equations for $H^+$ , $H^-$ , $H_2$ , $H_2^+$ , and $H_3^+$

Using the physical values and quantities from Sect. 3.5 the rate equation for ionized hydrogen may be written as

$$\begin{aligned}
\frac{\partial N_{H^+}}{\partial t} = & -\frac{N_{H^+}}{t_{\text{exp}}} + \sum_{k=1}^{15} R_{k,c}^{\gamma} \\
& + \sum_{k=1}^{15} N_{H^0,k} P_k - N_{H^+} N_e \sum_{k=1}^{15} \alpha_k \\
& + N_e \sum_{k=1}^{15} N_{H^0,k} q_{k,c} - N_{H^+} N_e^2 \sum_{k=1}^{15} q_{c,k} \\
& + (k_1 + k_2) N_{H^0}^2 + k_{13} N_{H^0} N_{H_2} \\
& + k_{22} N_{H_2}^+ N_{H^0} + k_{24} N_{H_2}^+ N_{H_2} + k_{27} N_{H_3}^+ N_{H_2} \\
& + k_{OH} N_{O^+} N_{H^0} + (R_4 + 2R_5) N_{H_2}^+ \\
& - k_{19} N_{H^+} N_{H^0} - (k_{20} + k_{21}) N_{H^+} N_{H_2} \\
& - (k_{28} + k_{29}) N_{H^-} N_{H^+} - k_{HO} N_{H^+} N_{O^0}, \tag{C.1}
\end{aligned}$$

where  $R_4$  and  $R_5$  are the photodissociation and dissociative photoionization rates evaluated with the relevant cross sections from Table B.5, respectively; the rate coefficients for the involved reactions are taken from Tables B.1–B.3. The rate equation for negative hydrogen ion is

$$\begin{aligned}
\frac{\partial N_{H^-}}{\partial t} = & -\frac{N_{H^-}}{t_{\text{exp}}} + N_{H^0} N_e \alpha_{H^-} - N_{H^-} P_{H^-} \\
& + k_2 N_{H^0}^2 + k_{11} N_{H^0} N_{H_2} + k_{33} N_e N_{H_2} \\
& - (k_{17} + k_{18}) N_{H^-} N_{H^0} - k_{30} N_{H^-} N_{H_2}^+ \\
& - (k_{28} + k_{29}) N_{H^-} N_{H^+} - k_{31} N_e N_{H^-}, \tag{C.2}
\end{aligned}$$

where  $\alpha_{\text{H}^-}$  and  $P_{\text{H}^-}$  are the total coefficient of photo-attachment of neutral hydrogen and electron to negative hydrogen ion and the photo-detachment rate of negative hydrogen ion in the continuum radiation field, respectively; the rate coefficients for the corresponding reactions are taken from Tables B.1–B.4. The rate equation for molecular hydrogen  $\text{H}_2$  is given by

$$\begin{aligned} \frac{\partial N_{\text{H}_2}}{\partial t} = & -\frac{N_{\text{H}_2}}{t_{\text{exp}}} - (R_1 + R_2 + R_3)N_{\text{H}_2} \\ & + k_3 N_{\text{H}^0}^3 + k_4 N_{\text{H}^0}^2 N_{\text{H}_2} \\ & + k_8 N_{\text{H}^0,1} N_{\text{H}^0,2s} + k_9 N_{\text{H}^0,1} N_{\text{H}^0,2p} \\ & + k_{18} N_{\text{H}^-} N_{\text{H}^0} + k_{22} N_{\text{H}_2^+} N_{\text{H}^0} + k_{25} N_{\text{H}_3^+} N_{\text{H}^0} \\ & + k_{27} N_{\text{H}_3^+} N_{\text{H}_2} + k_{30} N_{\text{H}^-} N_{\text{H}_2^+} + k_{36} N_{\text{e}} N_{\text{H}_3^+} \\ & - (k_{10} + k_{11} + k_{12}) N_{\text{H}^0} N_{\text{H}_2} \\ & - k_{14} N_{\text{H}_2} N_{\text{H}^0} - (k_{15} + k_{16}) N_{\text{H}_2}^2 \\ & - (k_{20} + k_{21}) N_{\text{H}^+} N_{\text{H}_2} - k_{23} N_{\text{H}_2^+} N_{\text{H}_2} \\ & - (k_{32} + k_{33} + k_{34}) N_{\text{e}} N_{\text{H}_2}, \end{aligned} \quad (\text{C.3})$$

where  $R_1$ ,  $R_2$ , and  $R_3$  are the photoionization, direct photodissociation, and two-step photodissociation (the Solomon process) rates of molecular hydrogen  $\text{H}_2$  evaluated with the cross sections from Table B.5, respectively; the rate coefficients for

the involved reactions are taken from Tables B.1–B.4. Finally, the rate equations for molecular hydrogen  $\text{H}_2^+$  and  $\text{H}_3^+$  are

$$\begin{aligned} \frac{\partial N_{\text{H}_2^+}}{\partial t} = & -\frac{N_{\text{H}_2^+}}{t_{\text{exp}}} + R_1 N_{\text{H}_2} - (R_4 + R_5) N_{\text{H}_2^+} \\ & + (k_5 N_{\text{H}^0,2s} + k_6 N_{\text{H}^0,2p} + k_7 N_{\text{H}^0,3}) N_{\text{H}^0} \\ & + (k_{11} + k_{12}) N_{\text{H}^0} N_{\text{H}_2} + k_{15} N_{\text{H}_2}^2 \\ & + k_{19} N_{\text{H}^+} N_{\text{H}^0} + k_{21} N_{\text{H}^+} N_{\text{H}_2} + k_{25} N_{\text{H}_3^+} N_{\text{H}^0} \\ & + k_{26} N_{\text{H}_3^+} N_{\text{H}_2} + k_{29} N_{\text{H}^-} N_{\text{H}^+} + k_{34} N_{\text{e}} N_{\text{H}_2} \\ & - k_{22} N_{\text{H}_2^+} N_{\text{H}^0} - (k_{23} + k_{24}) N_{\text{H}_2^+} N_{\text{H}_2} \\ & - k_{30} N_{\text{H}^-} N_{\text{H}_2^+} - k_{35} N_{\text{e}} N_{\text{H}_2^+} \end{aligned} \quad (\text{C.4})$$

and

$$\begin{aligned} \frac{\partial N_{\text{H}_3^+}}{\partial t} = & -\frac{N_{\text{H}_3^+}}{t_{\text{exp}}} + k_{14} N_{\text{H}_2} N_{\text{H}^0} \\ & + k_{20} N_{\text{H}^+} N_{\text{H}_2} + k_{23} N_{\text{H}_2^+} N_{\text{H}_2} \\ & - k_{25} N_{\text{H}_3^+} N_{\text{H}^0} - (k_{26} + k_{27}) N_{\text{H}_3^+} N_{\text{H}_2} \\ & - (k_{36} + k_{37}) N_{\text{e}} N_{\text{H}_3^+}, \end{aligned} \quad (\text{C.5})$$

respectively.